A Multi-instrument Study of a Dipolarization Event in the Inner Magnetosphere

H. Matsui[1], R. B. Torbert[1], H. E. Spence[1], M. R. Argall[1], I. J. Cohen[2], M. B. Cooper[3], R. E. Ergun[4], C. J. Farrugia[1], J. F. Fennell[5], S. A. Fuselier[6,7], M. Gkioulidou[2], Yu. V. Khotyaintsev[8], P.-A. Lindqvist[9], C. T. Russell[10], R. J. Strangeway[10], D. L. Turner[2], H. Vaith[1], and J. R. Wygant[11]

[1]Space Science Center, University of New Hampshire, Durham, NH, USA
[2]The Johns Hopkins University Applied Physics Laboratory, Laurel, MD, USA
[3]Center for Solar-Terrestrial Research, New Jersey Institute of Technology, Newark, NJ, USA
[4]Laboratory for Atmospheric and Space Physics, University of Colorado, Boulder, CO, USA
[5]Space Sciences Department, The Aerospace Corporation, El Segundo, CA, USA
[6]Southwest Research Institute, San Antonio, TX, USA
[7]University of Texas at San Antonio, San Antonio, TX, USA
[8]Swedish Institute of Space Physics, Uppsala, Sweden
[9]Royal Institute of Technology, Stockholm, Sweden
[10]Department of Earth, Planetary, and Space Sciences, University of California, Los Angeles, CA, USA
[11]School of Physics and Astronomy, University of Minnesota, Minneapolis, MN, USA

Key Points:

- A dipolarization was observed during a conjunction of Magnetospheric Multiscale and Van Allen Probe B in the inner magnetosphere.
- A B_Z increase on a timescale of minutes was overlaid with those on a timescale of seconds.
- The inertial term and the Hall term sometimes played a role during B_Z increases on a timescale of seconds.

Corresponding author: H. Matsui, `hiroshi.matsui@unh.edu`

Abstract

A dipolarization of the background magnetic field was observed during a conjunction of the Magnetospheric Multiscale (MMS) spacecraft and Van Allen Probe B on 22 September 2018. The spacecraft were located in the inner magnetosphere at $L \sim 6 - 7$ just before midnight magnetic local time (MLT). The separation between MMS and Probe B was $\sim 1R_E$. Gradual dipolarization or an increase of the northward component B_Z of the background field occurred on a timescale of minutes. Since both MMS and Probe B measured similar gradual increases, the spatial scale was of the order of the separation between these two. On top of that, there were B_Z increases, and a decrease in one case, on a timescale of seconds, accompanied by large electric fields with amplitudes > several tens of mV/m. Spatial scale lengths were of the order of the ion inertial length and the ion gyroradius. The inertial term in the momentum equation and the Hall term in the generalized Ohm's law were sometimes non-negligible. These small-scale variations are discussed in terms of the ballooning/interchange instability (BICI) and kinetic Alfvén waves. It is inferred that physics of multiple scales was involved in the dynamics of this dipolarization event.

1 Introduction

A dipolarization of the background geomagnetic field or an increase of its northward component B_Z often occurs in the nightside magnetosphere during geomagnetic activities (Cummings et al., 1968; McPherron et al., 1973). The dipolarization events are caused by geomagnetic field reconfiguration by which field lines stretched tailward move back to a more dipolar shape. These events are typically associated with plasma injections from the magnetotail (Baker et al., 1979; Reeves et al., 1992). There are various spatial scales related to these events, such as the magnetohydrodynamic (MHD) scale and the ion scale.

Concerning dipolarization events on large spatial scales, MHD simulations have been performed by, e.g., Birn et al. (2011), which was described in Kepko et al. (2015). The scale size of the structure is of the order of R_E. The current flowing through the structure is mainly related to the pressure through the momentum equation. Region 1 (R1) and Region 2 (R2) field-aligned currents (FACs) flow at different locations of the structure, depending on magnetic local time (MLT) and radial distance. R1 current flows into or out of the ionosphere in the dawnside or the duskside of the structure, respectively,

away from the Earth, while R2 current flows out of or into the ionosphere in the dawnside or the duskside, respectively, near the Earth. A multi-spacecraft observation consistent with this configuration has been reported by, e.g., R. Nakamura et al. (2017).

The spatial scale of the dipolarization structures may also be small, of the order of the ion inertial length or the ion gyroradius, so that the actual configuration would be more complicated. Small-scale structures could be caused by the kinetic ballooning/interchange instability (BICI). There are various simulations which reproduce this type of small-scale structures. Such examples are a Hall MHD simulation (Huba et al., 1987), a hybrid simulation (Winske, 1996) and a particle-in-cell (PIC) simulation (Pritchett & Coroniti, 2010). Although the above studies may not be specific to the dipolarization events or the BICI, the underlying physics is expected to be the same. The former two simulations did not examine the BICI but the Rayleigh-Taylor instability, in which the gradient B/curvature drift in the BICI is replaced by the gravitational drift. Ion-scale observations implying the BICI have been reported by Saito et al. (2008) and Hwang et al. (2011). Another possible mode for the ion-scale structure is the kinetic Alfvén waves, which is due to finite gyroradius effect on the Alfvén waves. Hasegawa (1976) developed a theory on this in order to explain particle acceleration and formation of auroral arcs, which could be related to the dipolarization process. Van Allen Probes measured these waves during a dipolarization event (Chaston et al., 2014).

It has been reported that the particle pressure is larger before the dipolarization event, namely earthward side of the structure, rather than afterwards (e.g., Runov et al., 2011). As a result, the electric field due to the Hall term in the generalized Ohm's law appears around the front: $\boldsymbol{E} = -\boldsymbol{V}\times\boldsymbol{B}+\boldsymbol{J}\times\boldsymbol{B}/ne$, where $\boldsymbol{E}$ is the electric field, $\boldsymbol{V}$ is the bulk velocity of plasmas, $\boldsymbol{B}$ is the magnetic field, $\boldsymbol{J}$ is the current density, n is the number density, and e is the electric charge. The second term in the right-hand side corresponds to the Hall term. This Hall electric field is considered as the finite ion gyroradius effect at a sharp pressure gradient near the structure. The Hall effect has been measured by Time History of Events and Macroscale Interactions during Substorms (THEMIS) (Runov et al., 2011) and Magnetospheric Multiscale (MMS) (R. Nakamura et al., 2018).

As discussed, it is possible that there are various spatial scales in a dipolarization structure. The earthward reconnection flow originally including the MHD scale would be modified by the BICI with the ion scale (M. S. Nakamura et al., 2002). Therefore,

it is expected that the dipolarization structure originally propagating from the magnetotail is not laminar by the time when it arrives at the inner magnetosphere.

In this study, we analyze a dipolarization event ∼22:29 UT on 22 September 2018, measured by both MMS and Van Allen Probe B in the inner magnetosphere. The detailed features of the event, such as the balance of the momentum equation and the significance of the Hall term in the generalized Ohm's law, are examined. There was similarity in a B_Z increase on a timescale of minutes between MMS and Probe B but not on a timescale of seconds. The objective of this study is to examine this dipolarization event in detail, especially in terms of its shape, the momentum equation, and the generalized Ohm's law. Based on this analysis, possible spatial configuration and physical properties related to this event are discussed. This type of study benefits further understanding of the effect of the dipolarization on the dynamics of the inner magnetosphere and the magnetosphere-ionosphere (M-I) coupling.

Note that each dipolarization signature is identified by a B_Z increase instead of a magnetic inclination increase in this study. This is because the spacecraft were located near the magnetic equator so that the inclination changes were relatively small (e.g., Ohtani, 1998). If the spacecraft is located right at the equator, then there would not be any inclination change. Otherwise, a slight change of the radial component in the cylindrical coordinates leads to an inclination change larger than that of the northward component. This radial component value would depend on the low latitude of the spacecraft position relative to the center of the injection region. Note that we also examine one B_Z decrease on a short timescale, which will be inferred to have physical properties similar to those of a B_Z increase.

This study is organized as follows. In Section 2, we explain the data set we analyze and spacecraft orbits. In Section 3, we examine the MMS measurement of a B_Z increase on a timescale of minutes, followed by B_Z increases and a decrease on a timescale of seconds. The Van Allen Probe observations are described in a similar manner in Section 4. MMS and Van Allen Probe data are compared to infer spatial configuration of the large-scale structure in Section 5, followed by discussion of possible physical mechanisms of the small-scale structures. Finally, summary and conclusions are presented (Section 6).

2 Data and Orbits

2.1 Data

In this study, we analyze MMS data (Burch et al., 2016). MMS consists of four spacecraft with identical instrumentation. There are various instruments measuring fields and particles. High time-resolution data are available, especially during burst-mode periods.

Electric field data were obtained by Electric Field Double Probes (EDP) (Ergun et al., 2016; Lindqvist et al., 2016). The sampling frequency is 32 Hz for the analyzed data. The data are shown in the Solar Magnetospheric (SM) coordinates unless otherwise noted because background, geomagnetic field is dominant. Note that electric field amplitudes of tens of mV/m discussed later are much larger than typical offset values $<\sim$ mV/m. Magnetic field data were obtained by Fluxgate Magnetometers (FGM) (Russell et al., 2016). The sampling frequency is 16 Hz. Since there are four MMS spacecraft, multi-spacecraft data analyses such as the timing analysis (e.g., Décréau et al., 2005), deriving normal motion of structures, and the curlometer technique (e.g., Dunlop & Eastwood, 2008), deriving current density, may sometimes work and are applied to these data.

Energetic protons were measured by Energetic Ion Spectrometer (EIS) (Mauk et al., 2016). The measured energy ranges are between $\sim$ 10 and several tens of keV for MCP-Pulse-Height by Time-of-Flight (PHxTOF) data and between several tens of keV and $\sim$ 1 MeV for Energy by Time-of-Flight (ExTOF) data. The lowest energy of $\sim$ 10 keV indicates that the major part of plasmasheet populations were measured by this instrument for the event shown here in the inner magnetosphere. Burst-mode and survey-mode data with the sampling periods of 0.6 s and 2.5 s, respectively, are analyzed. Energetic electrons were measured by Fly's Eye Electron Proton Spectrometer (FEEPS) (Blake et al., 2016). The energy range of the instrument is between several tens and several hundreds of keV. Here we analyze burst-mode and survey-mode data with the sampling periods of 0.3 s and 2.5 s, respectively. Lower energy protons with energy between a few eV and 40 keV were measured by the Hot Plasma Composition Analyzer (HPCA) (Young et al., 2016). The sampling period is $\sim 30-40$ s at the longest. The flux shown below is averaged over the full field of view.

We also analyze Van Allen Probes data (Mauk et al., 2013). Van Allen Probes performed comprehensive field and particle measurements in the inner magnetosphere. Al-

though there were two probes, A and B, we only analyze the latter data because of its proximity to MMS for the interval studied here.

Electric fields were measured by Electric Field and Waves (EFW) instrument (Wygant et al., 2013) on Probe B. Two components of electric fields sampled in the spin plane are analyzed. The third component along the spin axis is estimated with an assumption of $\boldsymbol{E} \cdot \boldsymbol{B} = 0$. The sampling frequency was 32 Hz. Magnetic fields were measured by the Fluxgate Magnetometers (MAG) (Kletzing et al., 2013). The sampling frequency was 64 Hz.

Energetic protons were measured by Radiation Belt Storm Probes Ion Composition Experiment (RBSPICE) between several tens and several hundreds of keV (Mitchell et al., 2013). The sampling period of TOF x Energy Hydrogen Rates data analyzed here was 0.3 s. Energetic electrons were measured by Magnetic Electron Ion Spectrometer (MagEIS) between a few tens and several hundreds of keV (Blake et al., 2013). The sampling period was 11 s. Low-energy protons and electrons were measured by Helium, Oxygen, Proton, and Electron (HOPE) mass spectrometer between ~ 1 eV and several tens of keV (Funsten et al., 2013). The sampling period was 22 s.

One advantage of analyzing this event is that MMS acquired burst-mode data in the inner magnetosphere. Energetic particle data are available with high time resolution. HPCA was also operated, although with more limited time resolution. However, the Fast Plasma Investigation (FPI) data (Pollock et al., 2016) are not available, so that some physical quantities, such as ion bulk velocity and electron pressure, may not be derived. In addition to FPI, there are no Electron Drift Instrument (EDI) data (Torbert et al., 2016), so that electron fluxes at 500 eV are not available. Lower time resolution and single-point measurements placed restrictions on the Van Allen Probes data analyses, as well.

2.2 Orbits

There was a dipolarization event measured in conjunction by MMS and Van Allen Probe B ∼22:29 on 22 September 2018. Left panels of Figure 1 show locations of MMS 1 and Probe B. Both spacecraft were at $L \sim 6 - 7$ in the premidnight MLT. Probe B was located $\sim 1 R_E$ closer to the Earth than MMS 1. MLTs of both spacecraft were similar.

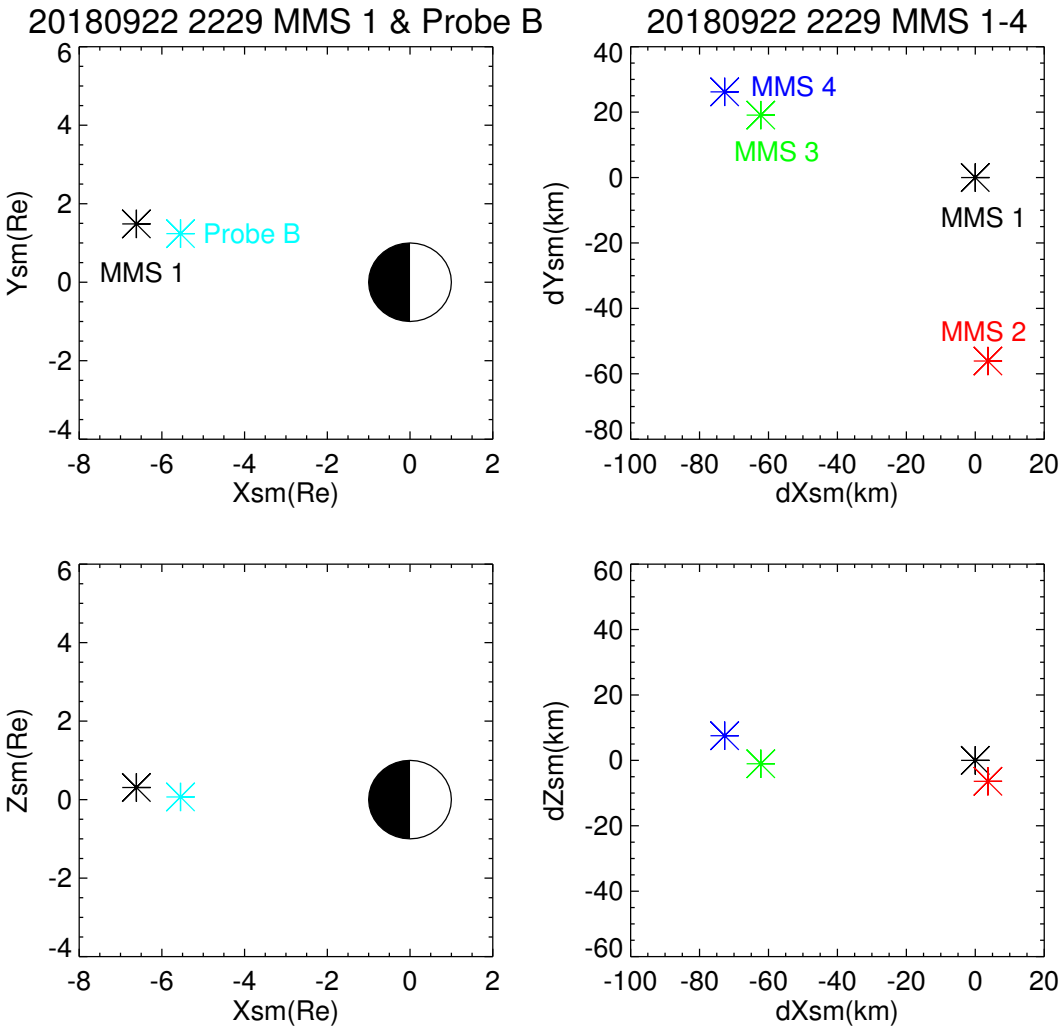

Figure 1. Left two panels show locations of MMS 1 and Van Allen Probe B in SM coordinates at 22:29 UT on 22 September 2018. Right two panels show locations of each MMS spacecraft relative to MMS 1 at the same time.

Locations of each MMS spacecraft relative to MMS 1 are shown in the right panels. Inter-spacecraft distances between each MMS spacecraft were < several tens of km, which approximately corresponds to the sub-ion scale. Therefore, ion-scale features analyzed in this study are expected to be captured well in the data set. Note that the spacecraft did not form an ideal tetrahedron because the spacecraft were far away from the apogee. The separation distances in the Z direction were small compared to other directions so that multi-spacecraft data analyses may not effectively work in this direction. Therefore, we have applied two methods to estimate the current density: the curlometer technique and comparison of magnetic fields between two spacecraft. In the latter

method, the spatial derivative in the X direction is estimated by comparing quantities between MMS 1 and 3, while the derivative in the Y direction is estimated from MMS 1 and 2. The spatial derivative in the Z direction, approximately aligned to the background magnetic field direction, is assumed to be small and therefore neglected. Below we present curlometer results except J_X or $(J\times B)_Y$, which are not consistent with those from the latter technique.

3 MMS Observations

In this section, we analyze a dipolarization event ∼22:29 on 22 September 2018, measured by MMS. Note that there was a small geomagnetic storm on this date. The minimum Dst −48 nT was recorded at 3 UT. The event was measured during the recovery phase. K_p index was moderate with 4^-. The Z component of the interplanetary magnetic field (IMF B_Z) in the OMNI data (King & Papitashvili, 2005) turned from northward to southward around the time when the B_Z increase was measured by MMS.

3.1 Overview and a Large-scale B_Z Increase Event

Figure 2 is an overview plot of electric and magnetic fields measured by MMS during a dipolarization event. There was a gradual B_Z increase at ∼22:27–31. Short timescale B_Z increases and decreases with a time scale of seconds were superposed on top of this gradual increase. During the gradual B_Z increase, the positive B_X component decreased, implying that the magnetic inclination increased. Note that the observations were made near midnight MLT. Therefore, the spacecraft were located at the northern side of the structure. This is consistent with the spacecraft location with the positive magnetic latitude (MLAT) of 2.6 deg. The center of the structure was likely located southward near the equator. The B_Y component increased ∼22:26:10–22:27:40, while decreased ∼22:27:40–22:28:30, which might correspond to upward R2 and downward R1 current on the dawnside of the structure, respectively. Here the current direction is referred at the ionosphere. However, there is some uncertainty in this estimation, due to large fluctuations in the time profile of the B_Y component.

Concerning the background electric field $E_{Y,DSL}$ in the DSL coordinates, the average and the standard deviation were 3.8±9.2 mV/m during the B_Z increase at 22:27–31, which were calculated from the data plotted in Figure 2. The DSL coordinates are

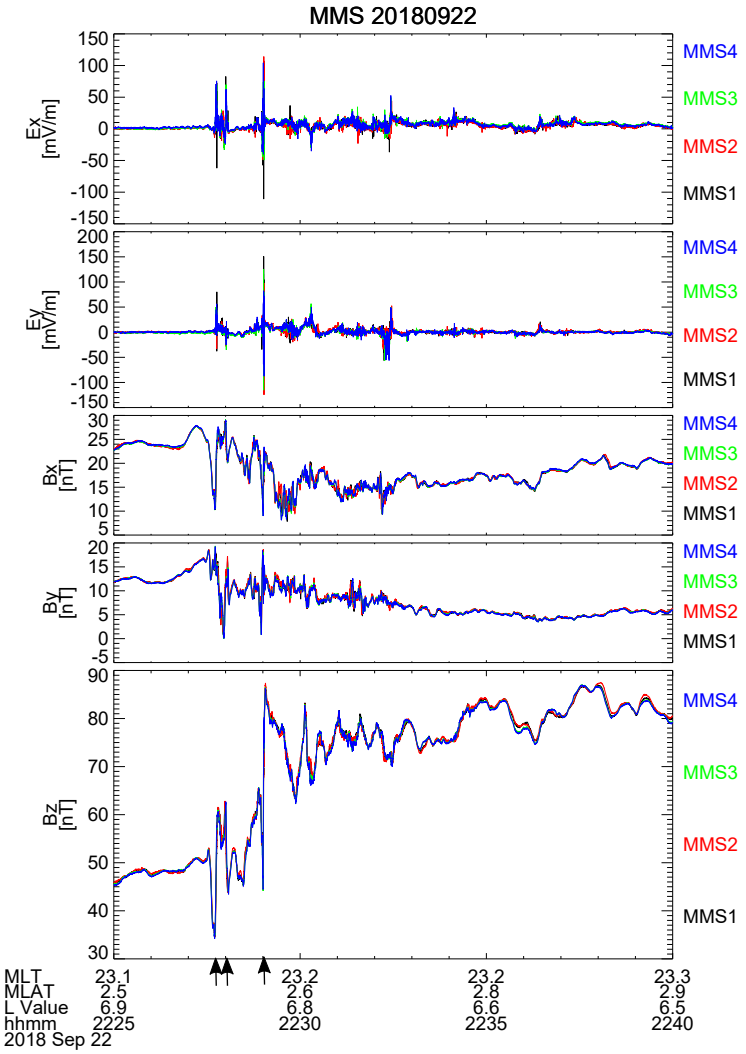

Figure 2. An overview plot of electric fields and magnetic fields between 22:25–40 on 22 September 2018. All MMS spacecraft data are overlaid, although most of them are on top of each other. Arrows in the bottom panel indicate when there were sporadic B_Z increases and a decrease, accompanied by large electric fields.

close to the geocentric solar ecliptic (GSE) coordinates. The Z_{DSL} axis points toward the spin axis of the spacecraft. The average value of $E_{X,DSL}$ is not shown here because there were offsets comparable to this value. Nonetheless, the above, large $E_{Y,DSL}$ value is fairly large compared to a typical value ~ 1 mV/m. Therefore, lots of magnetic fluxes were transported from the magnetotail toward the inner magnetosphere. Note that the standard deviation is even larger than the average value, indicating there were lots of fluctuations, some of which are the subject of the analysis below.

Next, we turn to short time-scale B_Z variations shown by arrows in the bottom panel. MMS measured the first B_Z increase at 22:27:43, followed by a decrease at 22:28:00.5. There was another large B_Z increase at 22:29:00.5. For each of these B_Z variations, there were large electric fields with amplitudes > several tens of mV/m. The amplitude was especially large, $\sim$ 100 mV/m, during the second B_Z increase.

Figure 3 shows an overview plot of particle data during the same interval as Figure 2. The proton flux > 100 keV is enhanced around short timescale B_Z increases. In contrast, the proton flux < several tens of keV decreased, possibly due to a lower value of the entropy parameter $P(\int \mathrm{d}l/B)^{5/3}$ (Wolf et al., 2006) than that of the surrounding area. Here, P is the plasma pressure, $\int \mathrm{d}l/B$ is the flux tube volume per unit magnetic flux, and l is the location along a magnetic field line. Similar flux changes depending on energy have been reported in the inner magnetosphere (Gkioulidou et al., 2015; Motoba et al., 2018). Gkioulidou et al. (2015) also found decreases of the entropy parameter after dipolarization. The energetic electron flux generally enhanced during the short timescale B_Z increases. The enhancement continued after these, which is clearer in electrons than protons. This is perhaps because electron motion would be rather adiabatic and/or electrons were locally accelerated by plasma waves such as chorus. Note that electrons < several tens of keV were not measured during this interval.

3.2 One Small-scale B_Z Increase Event

The second B_Z increase with a short timescale beginning at 22:29:00.5 is examined here in detail. As plotted in Figure 4, the B_Z component first started to slightly decrease $\sim$22:28:53. This signature was clearer after $\sim$22:28:56.5. Around this time, the B_Y and E_X components varied as well. Dawnward and southward current was observed. Energetic ion fluxes measured by MMS 2 started to decrease after $\sim$22:28:59. The B_Z component started to increase at 22:29:00.5, while energetic ion fluxes continued to decrease. The E_X component turned from negative to positive. The E_Y component was fluctuating, with both positive and negative values. Duskward and northward current was observed. Hereafter, the intervals during the B_Z decrease and the increase around the minimum B_Z value are mentioned as the dip and the dipolarization front (DF), respectively, following, e.g., Schmid et al. (2019). An interval including both the dip and DF is described as a single B_Z increase event because the B_Z increase is the main feature.

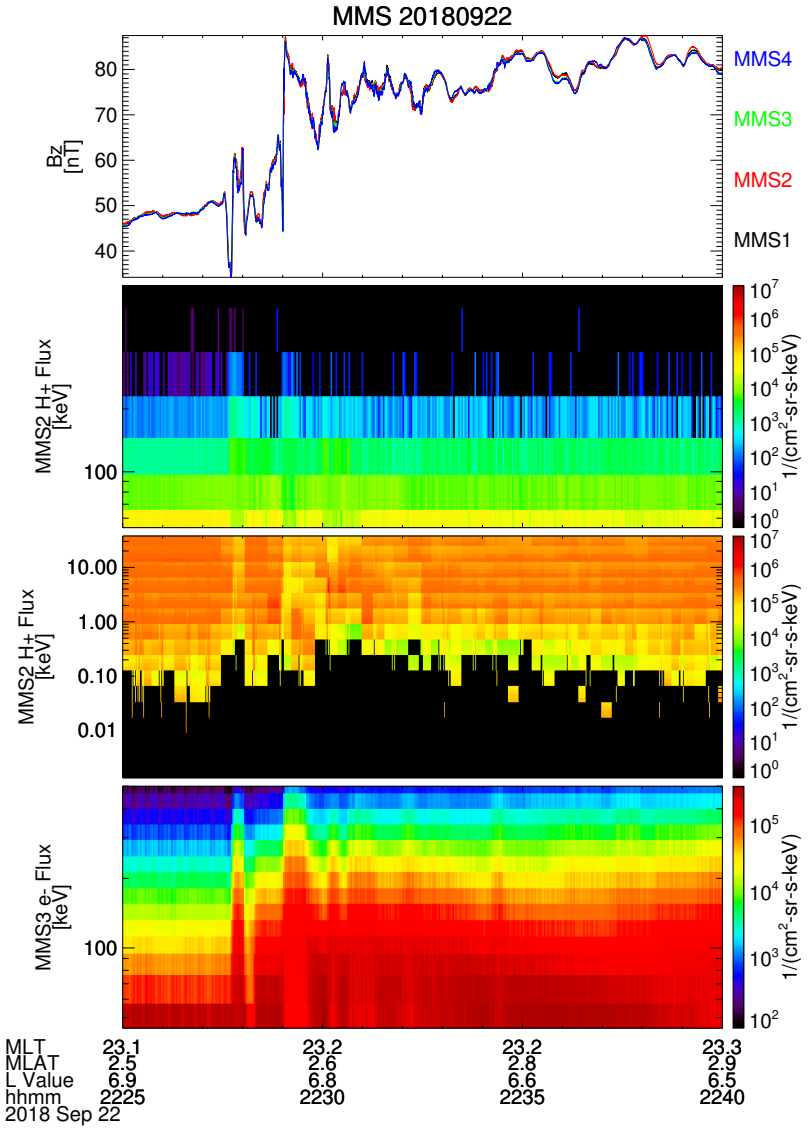

Figure 3. An overview plot of the particle flux together with the B_Z component between 22:25–40. Measurements of protons by EIS and HPCA and electrons by FEEPS are shown in the bottom three panels. EIS and HPCA data are plotted with the same color scale.

Since the inter-spacecraft separation between MMS 1 and 3 or MMS 1 and 4 was mainly in the X direction (Figure 1), the timing difference in each field component between these spacecraft indicates that the structure propagated earthward. The approximately concurrent timing between MMS 1 and 2, separated mainly in the Y direction with a similar distance to that between MMS 1 and 3, indicates that the normal direction of the propagation front did not have a large Y component. The timing analysis for three components of magnetic fields (Plaschke et al., 2016) during an interval including

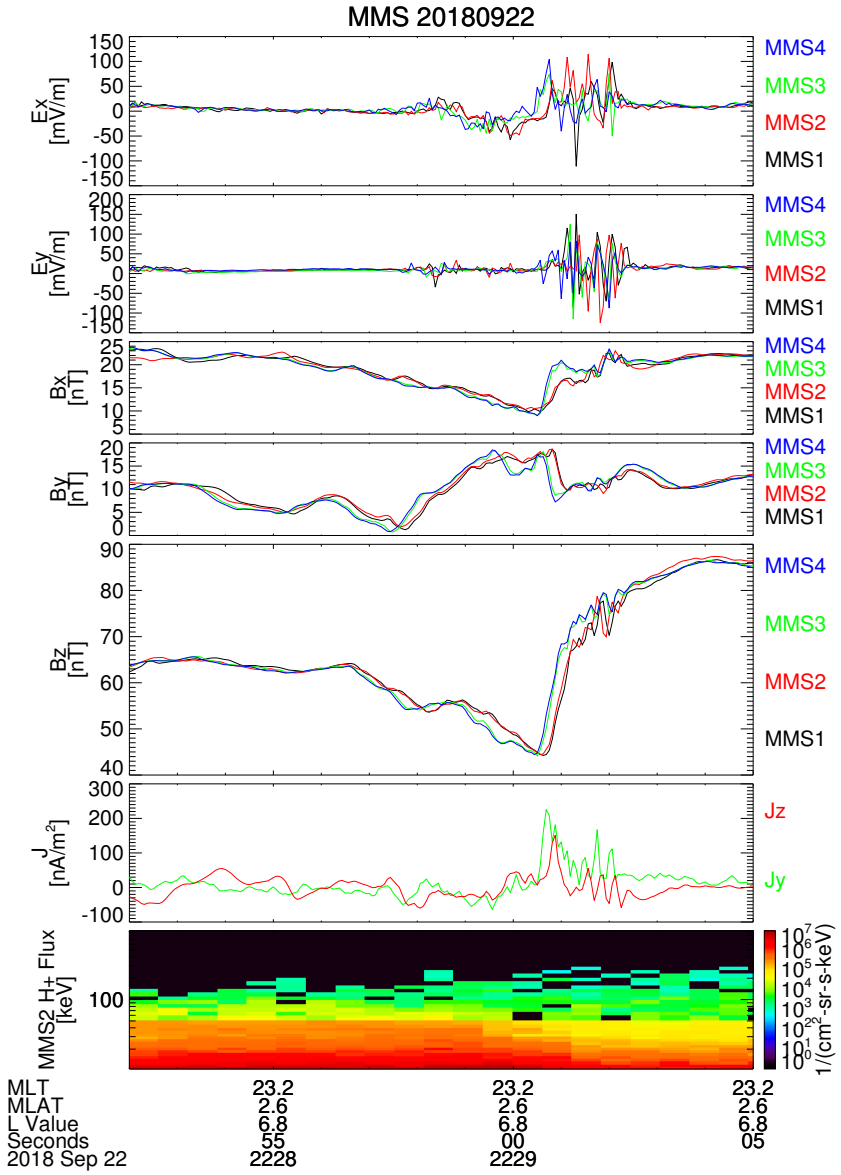

Figure 4. A detailed plot of the second B_Z increase with a short time-scale. Electric fields, magnetic fields, current density, and energetic ion fluxes from EIS are plotted.

the dip and DF between 22:28:56.5 and 22:29:04 yields a consistent result: the velocity in the normal direction V_N=230 km/s and the normal direction $\boldsymbol{N}$=(0.91, 0.24, 0.33). The structure primarily propagated earthward. Here the timing between each spacecraft pair is determined by that with maximum correlation between the original time-series and the lagged one. Variances or co-variances of all three components combined are calculated in order to derive the correlation coefficient.

Ion scale lengths in the dip are determined as follows: 150 km for the ion inertial length, 180 km for the ion gyroradius at an energy of 5 keV, and 570 km at an energy of 50 keV. Since the normal velocity was 230 km/s, these lengths correspond to time-series of the order of ~ 1 s, if the measured variation was not temporal but spatial. Energetic ion fluxes varied with this timescale. Here number density and magnetic field strength used for the calculation are 2.5 cm^{-3} and 58 nT, respectively. This density value is based on measurements by HPCA and PHxTOF with the energy below and above 10 keV, respectively, and calculated as a moment (See, e.g., Paschmann and Daly (1998)). Ion scale lengths in the DF are as follows: 230 km for the ion inertial length, 130 km for the ion gyroradius at an energy of 5 keV, and 420 km at an energy of 50 keV. These lengths correspond to time-series ~ 1 s. Variations in the time-series in the DF were of the order of this period. Here number density and magnetic field strength used for the calculation are 1.0 cm^{-3} and 79 nT, respectively.

Because of the finite gyroradius effect, the energetic ion flux does not depend only on the spacecraft location relative to the structure, but also on the gyrophase and thus the look direction of the instrument. In Figure 4, we show ion data from MMS 2 as a representative example. MMS 4 and 3 measured steeper or more gradual variations of the ion flux, respectively, while MMS 1 measured a similar slope (figure not shown).

Next, we discuss each term of the momentum equation, $\rho \mathrm{d}\boldsymbol{V}/\mathrm{d}t = \boldsymbol{J} \times \boldsymbol{B} - \nabla P$, in the X direction, referring to Figure 5. Here ρ is the mass density, P is the scalar pressure, and t is time. We consider scalar pressure instead of the pressure tensor, since there is more ambiguity in estimating that tensor. The left-hand side term $\rho \mathrm{d}V_X/\mathrm{d}t$ is unknown because the ion bulk velocity $\boldsymbol{V}$ is not measured with enough time resolution. It is also not so straightforward to derive the total time derivative. Concerning the terms in the right-hand side of the equation, the $(J \times B)_X$ term in the tailward direction in the dip before 22:29:00.5 (third panel) is inferred to be opposite to the $\partial P/\partial X$ term in the earthward direction, when we refer to the energetic proton flux decrease in the time-series (fourth panel). Here we have assumed that the approximately time-stationary structure moved earthward as determined by the timing analysis. Therefore, the inertial term $\rho \mathrm{d}V_X/\mathrm{d}t$ may point tailward so that the earthward moving plasma was decelerated.

After 22:29:00.5 in the DF, the $(J \times B)_X$ term turned positive, while the sign of the $\partial P/\partial X$ term did not change, implying both terms pointed toward the Earth. Nonethe-

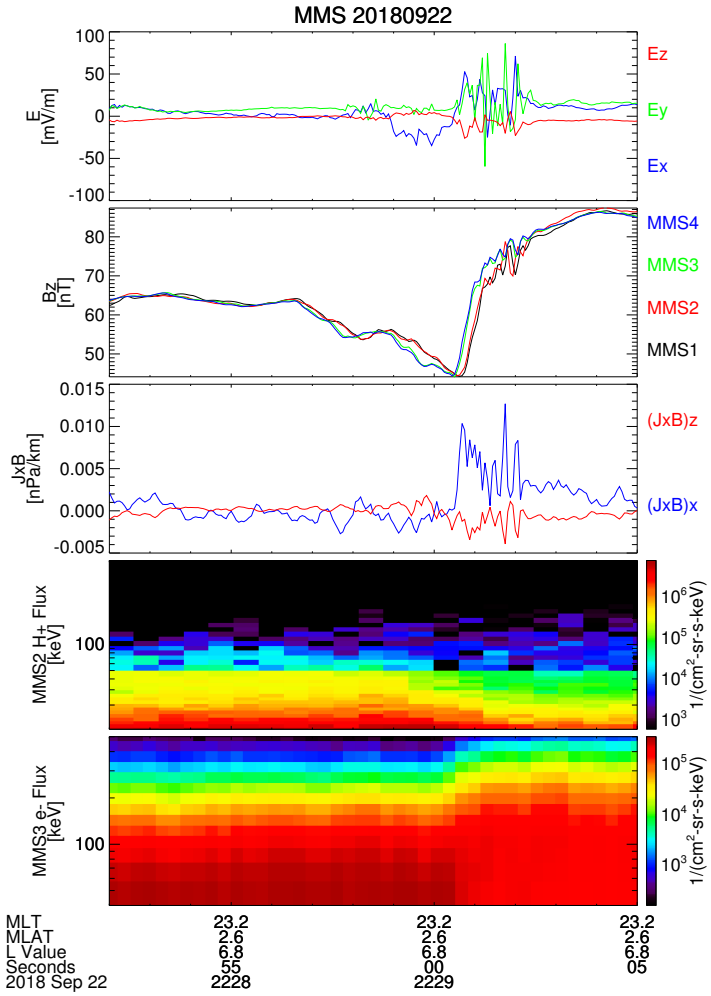

Figure 5. A detailed plot of the second B_Z increase with a short time-scale. The electric field, the B_Z component, two components of $\boldsymbol{J} \times \boldsymbol{B}$, energetic proton fluxes from EIS, and energetic electron fluxes from FEEPS are shown. The electric field is the average of data from all spacecraft, while the $\boldsymbol{J} \times \boldsymbol{B}$ term is based on the curlometer result and the magnetic field averaged for all spacecraft.

less, it is inferred that the $(J \times B)_X$ term was larger than the $\partial P/\partial X$ term, if the structure was primarily variable in the X direction. This is because the increase of the magnetic pressure was larger than the decrease of the pressure moment derived from the ion flux value. The $\rho \mathrm{d}V_X/\mathrm{d}t$ term could be positive, so that the earthward moving plasma was accelerated. Note that the azimuthal current and the radial electric field in the dip were in the opposite direction to those in the DF, respectively, so that they may partly cancel each other. In summary, the $(J \times B)_X$ term is possibly different from the $\partial P/\partial X$

term in the momentum equation. The inertial term $\rho \mathrm{d}V_X/\mathrm{d}t$ may not be zero so that the structure was not stationary in time. The time-series of magnetic fields were not always similar between spacecraft, e.g., the B_Y component at 22:29:00 and the B_X component at 22:29:01 (Figure 4), which could be due to the time variation of the structure related to the finite inertial term.

We then turn to each term of the generalized Ohm's law: $\boldsymbol{E} = -\boldsymbol{V} \times \boldsymbol{B} + \boldsymbol{J} \times \boldsymbol{B}/ne - \nabla P_e/ne$, where P_e is the electron pressure. Here the electron pressure term is included because we will consider whether this term was not negligible. The E_X component in the top panel of Figure 5 is compared with the $(J \times B)_X$ term in the third panel around when B_Z started to increase at 22:29:00.5. The electric field plotted is the average of all spacecraft data so that the comparison with the $(J \times B)_X$ term derived from the curlometer technique is facilitated. Both E_X and $(J \times B)_X$ terms were negative in the dip, while these turned positive in the DF. When we introduce the density mentioned before, $E_X \sim -7$ mV/m is inferred to be different from $(J \times B)_X/ne \sim -2$ mV/m on average before 22:29:00.5 in the dip, implying that the electric fields were approximately contributed by the $-(V \times B)_X$ term. Note that we do not have velocity data with enough time resolution so that the E_X component may not be directly compared with the $-(V \times B)_X$ term. After 22:29:00.5 in the DF, both $E_X \sim 18$ mV/m and $(J \times B)_X/ne \sim 24$ mV/m were positive with similar magnitudes on average so that the E_X component is inferred to be composed of the Hall term. One possible generation mechanism of the Hall electric field is the ion pressure difference between the dip and the DF. Such difference is not sharp enough but smoothed because of the finite ion gyroradius effect. These ions generate westward current and earthward electric field on the spatial scale of the ion gyroradius due to charge separation between ions and electrons (Runov et al., 2011). We actually measured gradual decrease of energetic ions on the spatial scale of the gyroradius, together with current and electric fields in the directions mentioned above.

Nonetheless, it is still possible that the $-(V \times B)_X$ term contributed to the generalized Ohm's law in the DF. We cannot confirm this because there are no velocity data with enough time resolution. Concerning the $-(\partial P_e/\partial X)/ne$ term, it is hard to show whether this term contributed to the generalized Ohm's law. The electron flux $>\sim 100$ keV increased in the DF, while this was the opposite at lower energy. Electron pressure

variations inferred from these high energy measurements were smaller than those of ions. In addition, we do not have electron measurements $<\sim$ 40 keV.

Note that contribution of oxygen to density or pressure is neglected in the above estimation because the oxygen/hydrogen ratio for these quantities was not large, $< 7\%$, at 22:27–31. Concerning Van Allen Probe data presented in the later section, the oxygen/hydrogen ratio was $< 16\%$. The contribution of oxygen is again neglected.

We next consider azimuthal plasma motion, approximately in the Y direction. There are two terms related to this motion: the inertial term $\rho \mathrm{d}V_Y/\mathrm{d}t$ in the momentum equation and the $-(V \times B)_X \sim -V_Y B_Z$ term in the generalized Ohm's law. The inertial term $\rho \mathrm{d}V_Y/\mathrm{d}t$ is related to the $(J \times B)_Y$ term and the $\partial P/\partial Y$ term. The latter term $\partial P/\partial Y$ may not be estimated from the analysis of single spacecraft data, assuming a time-stationary condition. Nonetheless, this term would be small if the structure was primarily variable in the X direction or the normal direction so that the $(J \times B)_Y$ term could be balanced by the $\rho \mathrm{d}V_Y/\mathrm{d}t$ term. The $-(V \times B)_X$ term was related to the E_X component in the dip, as mentioned before. In the DF, the $-(V \times B)_X$ term may contribute to the generalized Ohm's law, together with the Hall term. Since the pressure gradient in the Y direction would be small, the azimuthal plasma movement is possibly related to Alfvén waves, carrying field-aligned currents.

In addition, the inertial term in the Y direction could be related to the E_Y component through the Hall term in the same direction. However, the measured electric field fluctuated in the X direction in the low frequency range $<\sim$ 1 Hz so that the fluctuation was likely linearly polarized. This polarization is expected when the frequency is sufficiently smaller than the ion cyclotron frequency, at which the polarization is circular (e.g., Stix, 1992). Note that the Alfvén waves are connected to the electromagnetic ion cyclotron waves as the frequency increases. Therefore, the Hall term in the Y direction may be neglected. Because velocity would fluctuate in the Y direction, magnetic fluctuation in the same direction was expected in this low frequency limit of Alfvén waves, which was measured among other components. In our event, the ion cyclotron frequency was ~ 1 Hz, which was not so different from the variations in time-series. Since the measured variations were linearly polarized, these variations in time-series would be spatial rather than temporal, so that the analysis assuming the time stationary condition, such as determining the pressure gradient, approximately holds.

3.3 A Pair of a Small-scale B_Z Increase Event and a Decrease Event

There was another B_Z increase and a decrease starting at 22:27:43 and 22:28:00.5, respectively (Figure 6), ~ 1 min before the B_Z increase discussed in the above section. These events are also characterized by large electric fields as the previous event. The amplitudes were several tens of mV/m. A timing analysis during the first B_Z increase including the dip and the DF between 22:27:33–47 yields the following: $\boldsymbol{N} = (0.77, 0.44, -0.46)$ and $V_N = 85$ km/s. A timing analysis including the B_Z decrease interval between 22:28:00.5–12 yields: $\boldsymbol{N} = (0.94, -0.09, -0.34)$ and $V_N = -88$ km/s. The front moved tailward. The area with larger B_Z values was located tailward as well as the preceding structure with the B_Z increase. Therefore, the DF may be measured before the dip in the time-series. The normal direction $\boldsymbol{N}$ during the first B_Z increase pointed more duskward than that during this B_Z decrease interval.

The estimation on the momentum equation and the generalized Ohm's law is partly similar to that of the event ~ 1 min later. In the DF, the $(J \times B)_X$ term in the third panel was positive. The proton flux $\sim$ several tens of keV in the DF was smaller than that in the dip (fourth panel) so that the $(J \times B)_X$ term and the $\partial P/\partial X$ term were both in the earthward direction in the DF, although we cannot necessarily confirm whether the inertial term was nonzero. Concerning the generalized Ohm's law, the $(J \times B)_X/ne$ term was similar to the measured electric field in the X direction in the DF, indicating that the measured electric field was contributed by the Hall term. During the DF of the B_Z increase event, $E_X \sim 20$ mV/m and $(J \times B)_X/ne \sim 23$ mV/m on average, while during the DF of the B_Z decrease event, $E_X \sim 15$ mV/m and $(J \times B)_X/ne \sim 22$ mV/m. The $(J \times B)_X/ne$ term was close to 0 in the dip. In addition, the electric field direction in the DF during both the B_Z increase and the decrease was nearly aligned with the normal direction. The E_Y component as well as the N_Y component were positive during the B_Z increase, while both the E_Y and N_Y components were slightly negative during the B_Z decrease. Therefore, this could be another indication that the measured electric field was contributed by the Hall term. The electron flux in the bottom panel did not likely contribute to the generalized Ohm's law. The spatial scale of these events was of the order of the ion scale length. Since the B_Z increase and the decrease were next to each other, we may expect that the spatial distance between these structures was also of the order of the ion scale length.

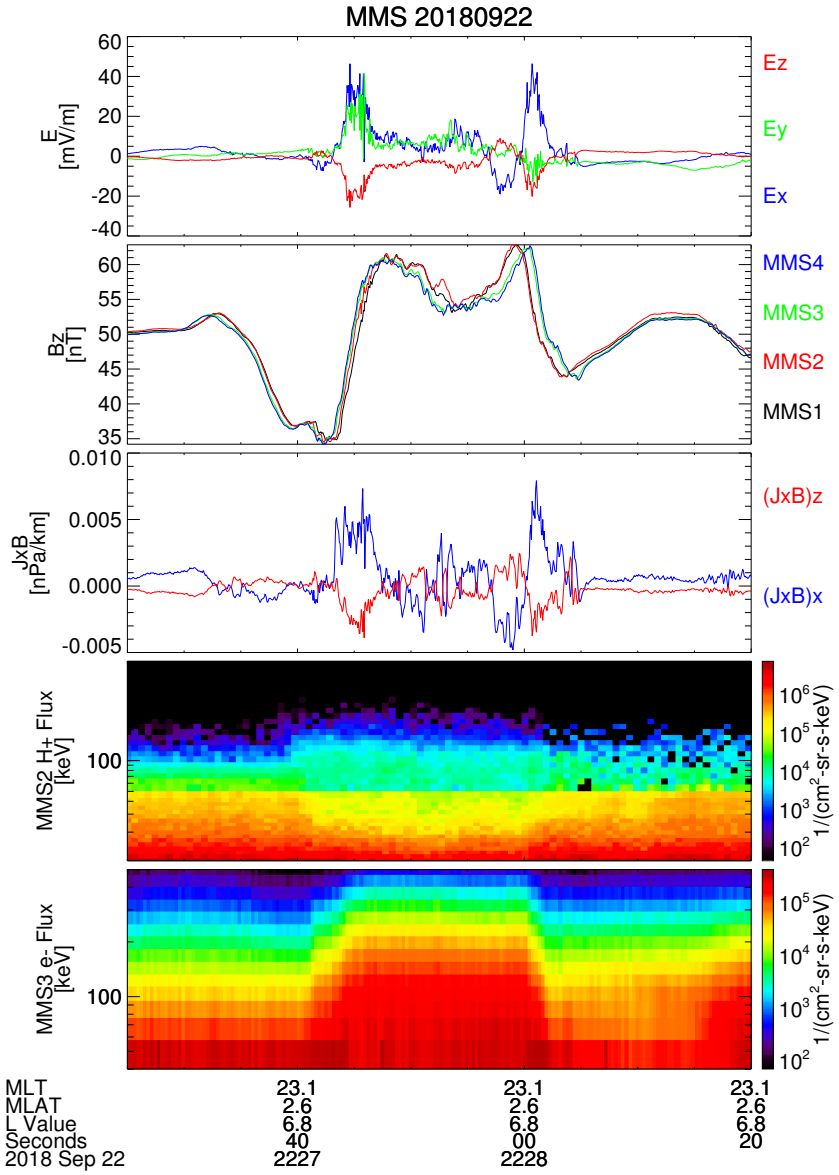

Figure 6. An overview plot of the first B_Z increase event and the decrease event on a timescale of seconds. The quantities plotted are the same as those in Figure 5.

4 Van Allen Probe Observations

4.1 Overview and a Large-scale B_Z Increase Event

Van Allen Probe B measured a B_Z increase on a timescale of minutes at a similar time as MMS did. Figure 7 shows magnetic field data between 22:25–40. During the B_Z increase, the B_X component also increased. If a typical dipolarization event occurs with the center of the structure located at the equator, then the $|B_X|$ value would de-

crease and the inclination would increase off the equator, both of which were not the case here. However, if the center of the structure would be slightly shifted northward, the increase of the measured B_X/B_Z ratio is consistent with that expected southward of the center of the structure. Note that the magnetic inclination does not change at the center of the structure. Since the MLAT of the spacecraft was 0.7 deg., smaller than 2.6 deg. of MMS, it was more probable that the center of the structure was shifted from the equator beyond the Probe B's position. Although the MLAT of Probe B was increasing, and hence the B_X/B_Z ratio of the background field should be as well, during the measurement, the increase of the measured ratio was larger than that of the dipole field. Therefore, the B_X/B_Z ratio was supposed to increase even at a fixed position for this event. However, the actual situation would be more complicated so that the above inference is merely one of the more simple possibilities. Concerning the B_Y component, the value increased and then decreased, which implies that the FACs flowed southward and northward, respectively. This was presumably due to the R2 and R1 currents duskward of the structure, respectively, connected to the southern ionosphere. On a shorter timescale of seconds, there was a B_Z increase at 22:29:55.5, indicated by an arrow.

Figure 8 is an overview plot of particle data during the same interval as Figure 7. Energetic proton fluxes at $\sim$ 100 keV were somewhat enhanced during the B_Z increase on a timescale of minutes. Lower-energy proton fluxes $<$ several tens of keV decreased. Overall, the flux variations were less clear than those of MMS. This is perhaps due to the entropy parameter $P(\int \mathrm{d}l/B)^{5/3}$ close to the neighboring values so that a bubble related to this dipolarization event was about to stop. Energetic electron fluxes $>\sim$ 10 keV generally enhanced at and after the short timescale B_Z increase at 22:29:55.5.

4.2 One Small-scale B_Z Increase Event

A detailed plot around the B_Z increase on a short timescale of seconds is shown in Figure 9. The B_Z component first decreased in the dip between 22:29:49–53 and then increased in the DF between 22:29:55.5–57. Large electric fields with amplitudes of several tens of mV/m, pointing earthward and dawnward, were measured in the DF. Concerning the normal direction of the structure, we perform the minimum variance analysis (MVA) (Paschmann & Daly, 1998) instead of the timing analysis because there were data from only one spacecraft. In order to perform the MVA using magnetic field data, first a co-variance matrix consisting of each pair of field components is constructed. Then,

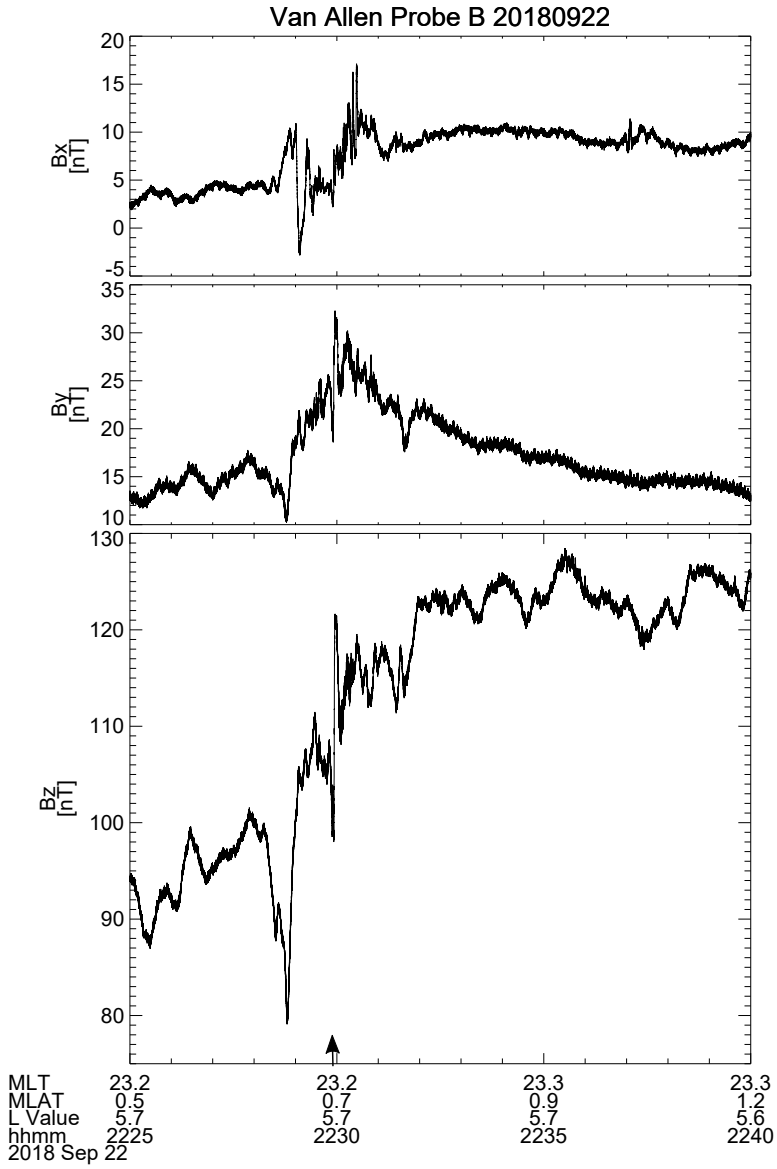

Figure 7. Magnetic field measurements by Van Allen Probe B during a dipolarization event. An arrow indicates a sporadic B_Z increase.

the matrix is diagonalized. The eigenvector with the minimum eigenvalue corresponds to the minimum variance direction. The MVA during an interval including both the dip and the DF yields $\boldsymbol{N} = (0.87, -0.48, 0.13)$ in the SM coordinates. Three eigenvalues of the analysis are 29, 4.4, and 0.11. The intermediate-to-minimum eigenvalue ratio is 40, which provides some credibility on the analysis. The normal direction was rather aligned along the X direction, the same as the MMS events. Since we cannot perform the timing analysis, the normal velocity V_N is assumed to be 200 km/s in the analyses below.

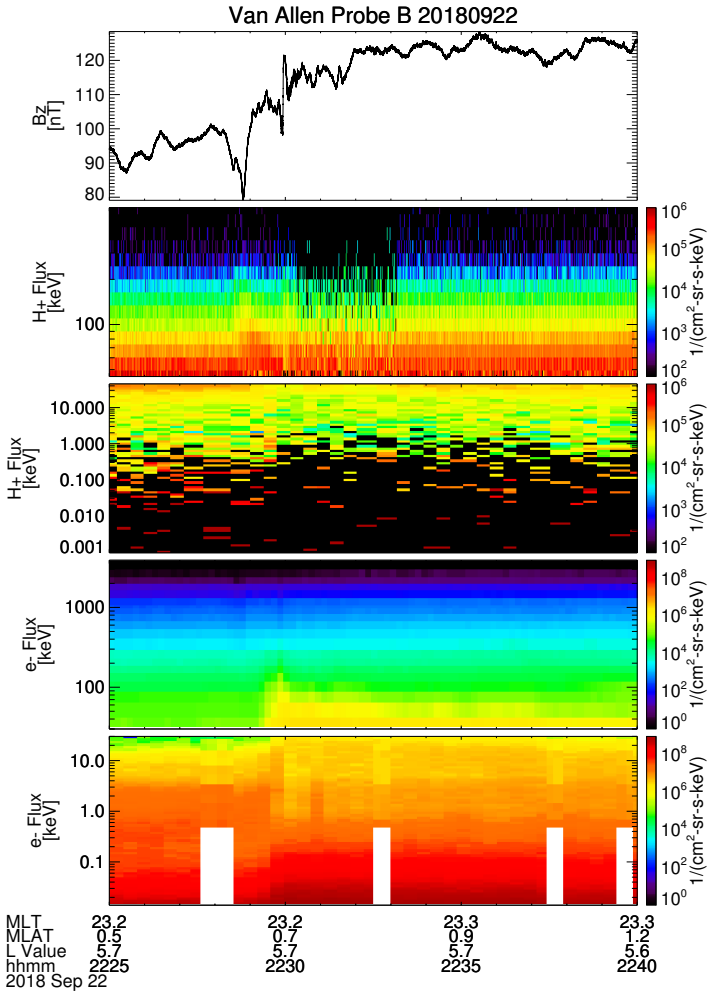

Figure 8. An overview plot of particle data measured by Van Allen Probe B between 22:25–40, including a dipolarization event. The B_Z component is plotted in the top panel as a reference. The second and third panels show proton fluxes from RBSPICE and HOPE, respectively, with a common color scale. The fourth and fifth panels show electron fluxes from MagEIS and HOPE, respectively, with a common color scale.

The ion inertial length for this event is approximately estimated as 300 km in both the dip and the DF, which corresponds to 1.5 s of time-series, assuming a time-stationary condition so that $\mathrm{d}N \sim -V_N \mathrm{d}t$. The lengths corresponding to the dip period of 4 s and the DF period of 1.5 s would be of the order of the above ion inertial length. Gyroradii of 50 and 500 keV ions are estimated to be 95 and 300 km, respectively, and would correspond to 0.5 and 1.5 s in time-series. These are of the same order of the dip and DF periods. The number density and the magnetic field strength used in this calculation are

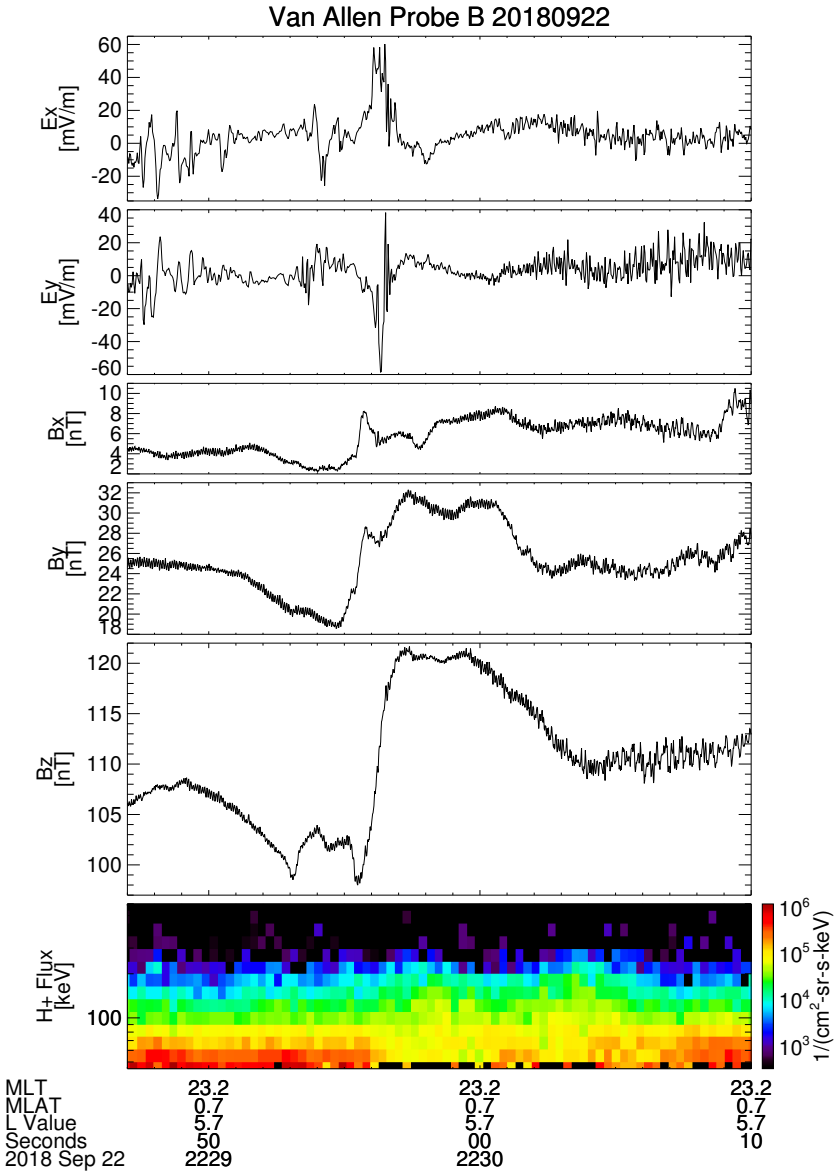

Figure 9. An overview plot of a short timescale B_Z increase measured by Van Allen Probe B. Electric fields, magnetic fields, and energetic proton fluxes from RBSPICE are plotted.

458 0.6 cm^{-3} and 110 nT, respectively, both in the dip and the DF. The number density is
459 based on electron moment data from the HOPE instrument with the energy between 200
460 eV and 50 keV. Therefore, there may be underestimation if there were many electrons
461 with the energy $<$ 200 eV. This was one possibility because the HPCA instrument on
462 MMS measured cold, dense plasmas $\sim$ 20 min after the large B_Z increase. At 22:52, the
463 spacecraft potential of MMS turned from positive to negative, when MMS was located
464 at L = 6.1 and 23.4 MLT. This MMS location was rather close to that of Probe B at

22:30. However, we cannot quantitatively estimate the cold plasma density at Probe B because of the somewhat different location and, more importantly, the different timing relative to the dipolarization event.

Next, we consider the balance of the momentum equation in the N direction, in which we may estimate the spatial gradient. Unlike MMS observations, the current density may not be calculated from the curlometer technique. The $(J \times B)_N$ term is approximated as $(J \times B)_N \sim -J_M B_Z \sim -(\partial B_Z/\partial N)B_Z/\mu_0 \sim (\partial B_Z/\partial t)B_Z/\mu_0 V_N$. Here μ_0 is the vacuum permeability and the M direction is that of the intermediate variation in the LMN coordinates as determined by the MVA. This M direction is perpendicular to the N direction and approximately in the $-Y$ direction. Thus, the $(J\times B)_N$ term is estimated as 0.0062 nPa/km in the DF. Around the minimum B_Z at 22:29:55.5, energetic ion flux $<\sim$ 70 keV decreased. If this decrease corresponded to the pressure decrease, the $\partial P/\partial N$ term is inferred to be in the same direction as the $(J\times B)_N$ term in the momentum equation in the DF. However, it is hard to quantitatively estimate how much pressure decreased due to the large fluctuations in fluxes. The effect of the low-energy ions $<\sim$ 40 keV, not measured by RBSPICE, to the pressure is expected to be small, when the pressure from HOPE is referred. We do not know how much the inertial term $\rho \mathrm{d}V_N/\mathrm{d}t$ contributed to the momentum equation.

Finally, we consider the balance of the generalized Ohm's law. The Hall electric field in the N direction is estimated as $\sim$ 65 mV/m, which is of the order of the measured $E_N \sim$ 27 mV/m, averaged over the DF period. Therefore, it is inferred that the Hall term contributed to the measured electric field. There are a couple of reasons for the discrepancy between these two quantities. Firstly, the $-(V \times B)_N$ term may not be negligible, although the moment velocity with enough time resolution is not available to confirm this. Secondly, if there were cold electrons as mentioned before, the above Hall electric field was likely overestimated. Lastly, the V_N value used in the above calculation was just an assumption. Nonetheless, the measured electric field in the earthward and dawnward direction was rather aligned along the normal direction of the structure, which might support the idea of the electric field contributed by the Hall term, as is also inferred in the MMS data analysis. In this case, the dawnward and tailward motion of field lines was rather parallel to the boundary between the dip and the DF or the M direction and not indicating the normal motion. Concerning the electron pressure gradient term, it is hard to examine whether this term contributed to the generalized Ohm's

law because electron measurements were not made with enough time resolution. In summary, the ion scale lengths, the momentum equation, and the generalized Ohm's law have been estimated as we performed in the MMS data analysis, although there are more constraints due to the single-spacecraft measurement. Nonetheless, the results are generally not inconsistent.

5 Discussion

5.1 Comparison between MMS and Van Allen Probe Observations

Figure 10 compares the B_Z component measured by MMS and Van Allen Probe B between 22:25–40. Both MMS and Probe B measured B_Z increases on timescales of minutes and seconds. On the one hand, the envelope of the B_Z increase is similar between MMS and Probe B at minute timescales. Both spacecraft were 1 R_E apart. Therefore, the gradual dipolarization itself would be large-scale with the scale length of the order of 1 R_E. As mentioned, MMS was possibly located dawnward of the structure, while Probe B was duskward. The center of the structure would be located between MMS and Probe B. Taking into account the background electric field measurements on a timescale of minutes by MMS, these structures propagated from the magnetotail toward the inner magnetosphere. Even though the background magnetic field strength was different between MMS and Probe B, the similar B_Z increase implies similar quantities of magnetic fluxes were transported. Since both MMS and Probe B were aligned in the radial direction, the contribution of the horizontal magnetic field difference between these two to the azimuthal current is estimated. The background dipole field is subtracted. Such westward current is calculated as 3 nA/m^2. In a similar manner, the horizontal current contributed by the azimuthal magnetic field difference between MMS and Probe B was calculated as -0.3 and 1 nA/m^2 before and after the dipolarization, respectively. It is inferred that the global R2 and R1 currents were measured in the northern hemisphere and the dawnside, taking into account that both spacecraft was located near midnight. Note that the current density estimated here is much smaller than that of the sporadic B_Z increase (Figure 4, although the area in which the global current is flowing is much wider.

On the other hand, there were sometimes sporadic B_Z increases and a decrease with ion scales, as examined in the previous sections and indicated by arrows in Figure 10.

These small-scale structures do not seem to correlate between MMS and Probe B. Therefore, the scale lengths of these structures were less than their separation distance, several tens of ion inertial lengths. Overall, small, ion-scale structures may overlay above the large, MHD-scale structure. Structures with each scale size would be consistent with simulation results of each size, described in the Introduction. Below we discuss the small-scale structures in more detail.

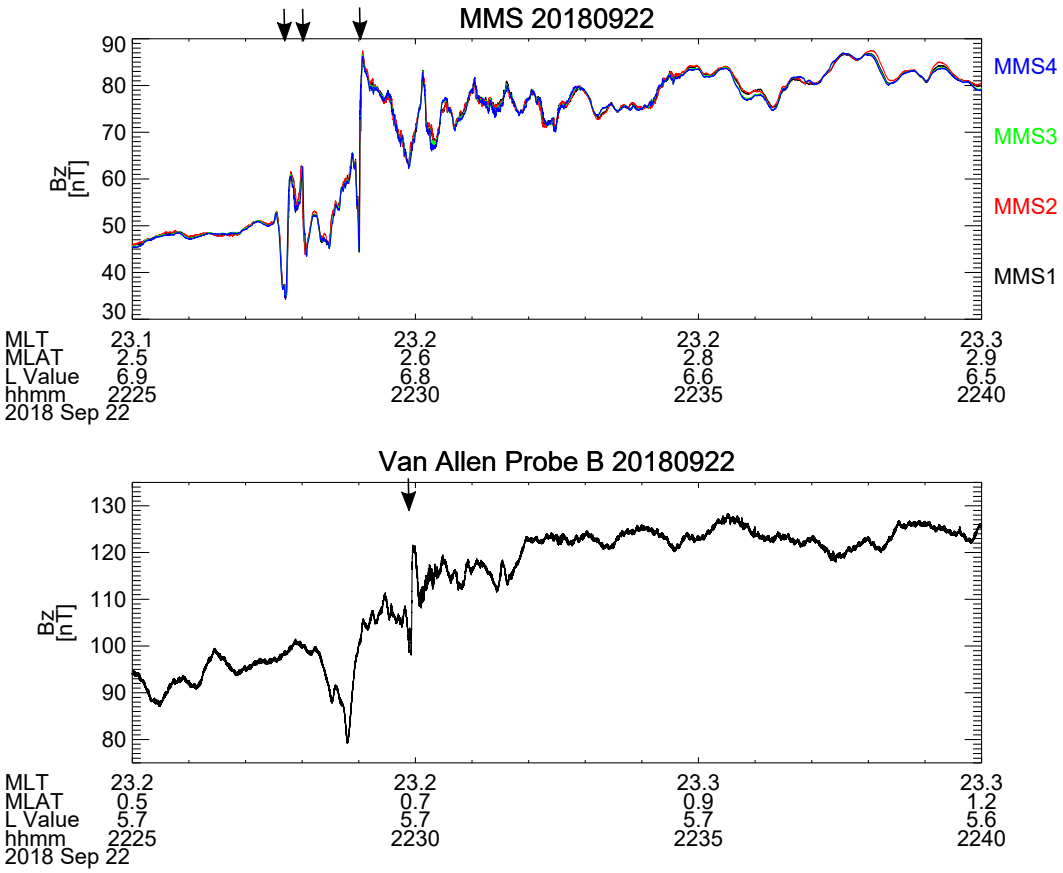

Figure 10. A plot comparing the B_Z component measured by MMS and Van Allen Probe B during a dipolarization event. Vertical arrows indicate B_Z increases and a decrease on a timescale of seconds, discussed in the previous sections.

5.2 Characteristics of Small-scale Structures

In this section, we discuss properties of small-scale structures. First, we consider the possibility of the ballooning/interchange instability (BICI) (e.g., Miura, 2007; Pritchett & Coroniti, 2010; Wolf et al., 2006, and references therein). The BICI usually occurs

when a geomagnetic flux tube with the larger entropy parameter $P(\int \mathrm{d}l/B)^{5/3}$ is located closer to the Earth. The difference between the ballooning instability and the interchange instability is whether the ionospheric foot point is not/is moving, respectively. We do not examine this difference here. The BICI is equivalent to the Rayleigh-Taylor instability, when the term due to the gradient B/curvature drift is replaced by the gravity term.

There are two features derived from our measurement. The first feature is the entropy parameter. As already described, the pressure decreased around where the B_Z component started to increase. Concerning the flux tube volume, we refer to an empirical formula of Wolf et al. (2006), as performed in Gkioulidou et al. (2015). It turns out that this volume does not change much between neighboring locations in the inner magnetosphere where the background magnetic field is large. Therefore, the entropy parameter in the dip is inferred to be larger than that in the DF. Second, the spatial scale of the small-scale variations was of the order of the ion gyroradius. The former feature on the entropy parameter generally satisfies the instability criterion of the BICI so that the BICI may grow at various spatial scales. Nonetheless, the growth rate would be larger during the linear stage when the scale length is of the order of the ion gyroradius (Pritchett & Coroniti, 2010; Winske, 1996). As noted, the scale length of the ion scale is the second feature of the measurement.

It is possible that the BICI was initiated in the deeper magnetotail at $X <\sim -10R_E$. If so, we may calculate propagation time of the dipolarization structure from the magnetotail to the spacecraft position. The background electric field of ~ 4 mV/m is based on the MMS measurement, while the magnetic field strength of several tens of nT is used for the calculation, together with a propagation distance of 3 R_E between $L = 10$ and 7. The estimated value is of the order of $\sim 100\omega_{ci}$, where ω_{ci} is the ion cyclotron frequency. This is generally in the nonlinear stage in numerical simulations (Pritchett & Coroniti, 2013; Winske, 1996), although it may be difficult to quantitatively compare simulations with measurements due to different parameters between these two. Nonetheless, we may expect the nonlinear feature such as the interchange head was measured.

Figure 11 depicts one possible MMS trajectory across the structure. Here only small-scale spatial variations possibly due to the BICI are depicted and the large-scale, MHD variations are neglected. The ambiguous portion is identified by dashed lines. The scale

size of the structure is of the order of the ion gyroradius. MMS first measured a B_Z increase and then a decrease soon after that. It is expected from the timing analysis that the region with large B_Z values (DF) was located tailward during both the B_Z increase and the decrease. In the figure, we also take into account the estimated normal directions of the structure. The N_Y value during the B_Z increase was larger than that during the decrease. The E_Y value was positive at the DF during the B_Z increase, while it was slightly negative during the decrease (Figure 6). As noted before, this different E_Y value would be associated with different normal directions of the structure, in which the Hall electric field was supposed to point. The measurement is also consistent with the simulation that there was a pair of E_Y signs in the interchange head (Pritchett & Coroniti, 2013). About 1 minute later, a B_Z increase was again observed. The interval between neighboring interchange heads would be longer than the width of each head during the nonlinear stage. This might explain that 1 minute time lag. Note that the above cartoon is a simplified picture. In reality, the electric field is not time-stationary or spatially homogeneous. The boundary between the dip and the DF may continuously deform because of variable normal motion between each B_Z increase and decrease as inferred from the timing analysis. In addition, there could be multiple DFs during a single dipolarization event on a time scale of minutes so that the boundary between the dip and the DF may not be continuous as depicted in the cartoon. Therefore, the detailed, actual configuration could be more complicated.

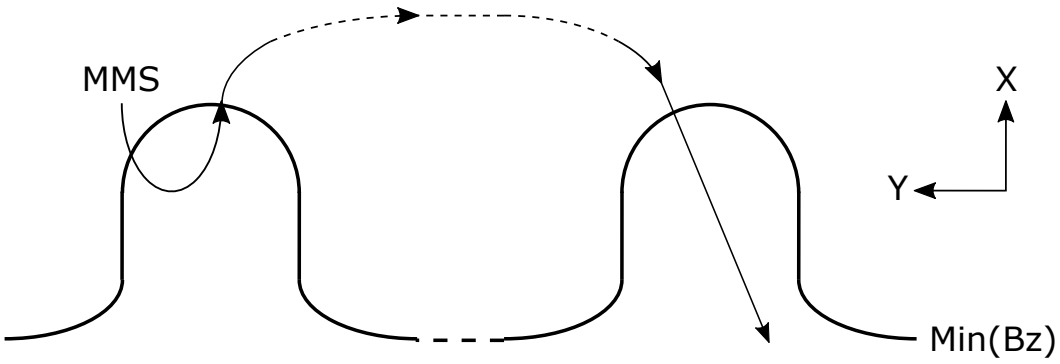

Figure 11. A possible MMS trajectory around the small-scale dipolarization structure. The location with minimum B_Z is indicated by a thick line, while the MMS trajectory is indicated by a thin line. Ambiguous portions are identified by dashed lines.

There are high β regions in the dusk to midnight sectors of the inner magnetosphere, which could satisfy the instability criterion of the mirror/drift-mirror mode (Cooper et al., 2018). However, this is not the case for the dipolarization event, measured by MMS and Probe B and analyzed in this study. In addition, the magnetic field strength decreased as the energetic ion flux decreased in the dip region of the second B_Z increase measured by MMS (Figure 4). The magnetic field strength and pressure variations were thus sometimes in phase, which is not expected for the mirror mode. Therefore, this mode is inferred to be unlikely at least for the event analyzed here.

Lastly, measured electromagnetic fluctuations could be due to kinetic Alfvén waves. This is because inertial terms may not be negligible and that the spatial scale of the variation was ion gyroradius. Large, earthward electric fields were measured in the DF. Part of these large electric fields may be contributed by the azimuthal plasma motion in addition to the Hall term. There ware large, tailward electric fields in the dip of the second B_Z increase recorded by MMS. Measured E_X and B_Y components could constitute Alfvén waves, accompanied by field-aligned currents. It has been suggested that surface waves may convert their mode to kinetic Alfvén waves (Chaston et al., 2007; Hasegawa, 1976). The fluctuation due to the BICI is considered as surface waves. Therefore, the two possible modes discussed here, BICI and kinetic Alfvén waves, are not necessarily independent, although the plasma condition discussed here may not be the same as those in the above references. Even though E_X and B_Y variations may be related to the Alfvén waves, phases of these components were shifted by ~ 90 degrees. At the time of the minimum B_Z, the B_Y value was maximum, while the E_X value changed signs. The E/B ratio was variable around the minimum B_Z. Therefore, measured variations are not inferred to be propagating waves but standing waves.

6 Summary and Conclusions

MMS and Van Allen Probe B were located in the premidnight inner magnetosphere $\sim$22:29 on 22 September 2018. The separation between MMS and Probe B was $\sim 1 R_E$ in the radial direction. Both spacecraft measured a dipolarization event. The large envelope of the B_Z increase was measured on a timescale of minutes, while there were sporadic B_Z increases and a decrease on a timescale of seconds on top of that, accompanied by large electric fields. The large-scale B_Z variation of the order of minutes was similar between MMS and Probe B. The spatial scale was as long as the distance between

these two. The center of this structure is inferred to be located in between, referring to B_X and B_Y components. During the DF of sporadic B_Z increases, the $(J\times B)_X$ term in the momentum equation was not necessarily balanced by the $\partial P/\partial X$ term, implying the presence of the inertial term, which could be opposite to that in the dip. The Hall term $(J\times B)_X/Ne$ in the DF may contribute to the generalized Ohm's law because its size was similar to that of the electric field. This is also inferred from the electric field direction close to the normal direction of the structure. The scale size of the small-scale structures was of the order of the ion inertial length and the ion gyroradius. Measurements of these structures by MMS and Probe B, separated by several tens of ion inertial lengths, were not similar. The small-scale structures would be excited by the kinetic BICI because of the small entropy parameter in the tailward direction and the ion scale of the structure. It is also possible that this structure was related to the kinetic Alfvén waves due to the presence of the inertial term and the ion scale. Therefore, it is inferred that physics of multiple scales was involved in the dynamics of this dipolarization event.

Acknowledgments

This work was supported by NASA's MMS contract NNG04EB99C and Van Allen Probes contract NAS5-01072. MMS data are publicly available at https://lasp.colorado.edu/mms/sdc/public/. Van Allen Probes data are available at http://www.space.umn.edu/missions/rbspefw-home-university-of-minnesota/, https://emfisis.physics.uiowa.edu/, https://rbspice.ftecs.com/, and http://www.RBSP-ect.lanl.gov/. Solar Wind OMNI data are available at https://omniweb.gsfc.nasa.gov/. *Dst* index is available at http://wdc.kugi.kyoto-u.ac.jp/. K_p index is available at https://www.gfz-potsdam.de/en/kp-index/.

References

Baker, D. N., Belian, R. D., Higbie, P. R., & Hones, E. W., Jr. (1979). High-energy magnetospheric protons and their dependence on geomagnetic and interplanetary conditions. *Journal of Geophysical Research*, *84*, 7138–7154. doi: https://doi.org/10.1029/JA084iA12p07138

Birn, J., Nakamura, R., Panov, E. V., & Hesse, M. (2011). Bursty bulk flows and dipolarization in MHD simulations of magnetotail reconnection. *Journal of Geophysical Research*, *116*, A01210. doi: https://doi.org/10.1029/2010JA016083

Blake, J. B., Carranza, P. A., Claudepierre, S. G., Clemmons, J. H., Crain, W. R., Jr., Dotan, Y., et al. (2013). The Magnetic Electron Ion Spectrometer (MagEIS) instruments aboard the Radiation Belt Storm Probes (RBSP) spacecraft. *Space Science Reviews*, *179*, 383–421. doi: https://doi.org/10.1007/s11214-013-9991-8

Blake, J. B., Mauk, B. H., Baker, D. N., Carranza, P., Clemmons, J. H., Craft, J., et al. (2016). The Fly's Eye Energetic Particle Spectrometer (FEEPS) sensors for the Magnetospheric Multiscale (MMS) mission. *Space Science Reviews*, *199*, 309–329. doi: https://doi.org/10.1007/s11214-015-0163-x

Burch, J. L., Moore, T. E., Torbert, R. B., & Giles, B. L. (2016). Magnetospheric Multiscale overview and science objectives. *Space Science Reviews*, *199*, 5–21. doi: https://doi.org/10.1007/s11214-015-0164-9

Chaston, C. C., Bonnell, J. W., Wygant, J. R., Mozer, F., Bale, S. D., Kersten, K., et al. (2014). Observations of kinetic scale field line resonances. *Geophysical Research Letters*, *41*, 209–215. doi: https://doi.org/10.1002/2013GL058507

Chaston, C. C., Wilber, M., Mozer, F. S., Fujimoto, M., Goldstein, M., Acuna, M., et al. (2007). Mode conversion and anomalous transport in Kelvin-Helmholtz vortices and kinetic Alfvén waves at the Earth's magnetopause. *Physical Review Letters*, *99*, 175004. doi: https://doi.org/10.1103/PhysRevLett.99.175004

Cooper, M. B., Gerrard, A. J., Soto-chavez, A. R., & Lanzerotti, L. J. (2018). High beta regions in the inner magnetosphere and their potential for ULF wave generation. In *American Geophysical Union, Fall Meeting 2018, SM51D-2763.*

Cummings, W. D., Barfield, J. N., & Coleman, P. J., Jr. (1968). Magnetospheric substorms observed at the synchronous orbit. *Journal of Geophysical Research*, *73*, 6687–6698. doi: https://doi.org/10.1029/JA073i021p06687

Décréau, P. M. E., Le Guirriec, E., Rauch, J. L., Trotignon, J. G., Canu, P., Darrouzet, F., et al. (2005). Density irregularities in the plasmasphere boundary layer: Cluster observations in the dusk sector. *Advances in Space Research*, *36*, 1964–1969. doi: https://doi.org/10.1016/j.asr.2005.08.050

Dunlop, M. W., & Eastwood, J. P. (2008). The curlometer and other gradient based methods. In G. Paschmann & P. W. Daly (Eds.), *Multi-spacecraft analysis methods revisited* (pp. 17–26). Noordwijk, The Netherlands: ESA Communica-

tions.

Ergun, R. E., Tucker, S., Westfall, J., Goodrich, K. A., Malaspina, D. M., Summers, D., et al. (2016). The Axial Double Probe and Fields Signal Processing for the MMS mission. *Space Science Reviews*, *199*, 167–188. doi: https://doi.org/10.1007/s11214-014-0115-x

Funsten, H. O., Skoug, R. M., Guthrie, A. A., MacDonald, E. A., Baldonado, J. R., Harper, R. W., et al. (2013). Helium, Oxygen, Proton, and Electron (HOPE) mass spectrometer for the Radiation Belt Storm Probes mission. *Space Science Reviews*, *179*, 423–484. doi: https://doi.org/10.1007/s11214-013-9968-7

Gkioulidou, M., Ohtani, S., Mitchell, D. G., Ukhorskiy, A. Y., Reeves, G. D., Turner, D. L., et al. (2015). Spatial structure and temporal evolution of energetic particle injections in the inner magnetosphere durng the 14 July 2013 substorm event. *Journal of Geophysical Research: Space Physics*, *120*, 1924–1938. doi: https://doi.org/10.1002/2014JA020872

Hasegawa, A. (1976). Particle acceleration by MHD surface wave and formation of aurora. *Journal of Geophysical Research*, *81*, 5083–5090. doi: https://doi.org/10.1029/JA081i028p05083

Huba, J. D., Lyon, J. G., & Hassam, A. B. (1987). Theory and simulation of the Rayleigh-Taylor instability in the limit of large larmor radius. *Physical Review Letters*, *59*, 2971–2974. doi: https://doi.org/10.1103/PhysRevLett.59.2971

Hwang, K.-J., Goldstein, M. L., Lee, E., & Pickett, J. S. (2011). Cluster observations of multiple dipolarization fronts. *Journal of Geophysical Research*, *116*, A00I32. doi: https://doi.org/10.1029/2010JA015742

Kepko, L., McPherron, R. L., Amm, O., Apatenkov, S., Baumjohann, W., Birn, J., et al. (2015). Substorm current wedge revisited. *Space Science Reviews*, *190*, 1–46. doi: https://doi.org/10.1007/s11214-014-0124-9

King, J. H., & Papitashvili, N. E. (2005). Solar wind spatial scales in and comparisons of hourly Wind and ACE plasma and magnetic field data. *Journal of Geophysical Research*, *110*, A02104. doi: https://doi.org/10.1029/2004JA010649

Kletzing, C. A., Kurth, W. S., Acuna, M., MacDowall, R. J., Torbert, R. B., Averkamp, T., et al. (2013). The Electric and Magnetic Field Instrument Suite and Integrated Science (EMFISIS) on RBSP. *Space Science Reviews*,

179, 127–181. doi: https://doi.org/10.1007/s11214-013-9993-6

Lindqvist, P.-A., Olsson, G., Torbert, R. B., King, B., Granoff, M., Rau, D., et al. (2016). The Spin-plane Double Probe electric field instrument for MMS. *Space Science Reviews*, *199*, 137–165. doi: https://doi.org/10.1007/s11214-014-0116-9

Mauk, B. H., Blake, J. B., Baker, D. N., Clemmons, J. H., Reeves, G. D., Spence, H. E., et al. (2016). The Energetic Particle Detector (EPD) investigation and the Energetic Ion Spectrometer (EIS) for the Magnetospheric Multiscale (MMS) mission. *Space Science Reviews*, *199*, 471–514. doi: https://doi.org/10.1007/s11214-014-0055-5

Mauk, B. H., Fox, N. J., Kanekal, S. G., Kessel, R. L., Sibeck, D. G., & Ukhorskiy, A. (2013). Science objectives and rationale for the Radiation Belt Storm Probes mission. *Space Science Reviews*, *179*, 3–27. doi: https://doi.org/10.1007/s11214-012-9908-y

McPherron, R. L., Russell, C. T., & Aubry, M. P. (1973). Satellite studies of magnetospheric substorms on August 15, 1968 9. Phenomenological model for substorms. *Journal of Geophysical Research*, *78*, 3131–3149. doi: https://doi.org/10.1029/JA078i016p03131

Mitchell, D. G., Lanzerotti, L. J., Kim, C. K., Stokes, M., Ho, G., Cooper, S., et al. (2013). Radiation Belt Storm Probes Ion Composition Experiment (RBSPICE). *Space Science Reviews*, *179*, 263–308. doi: https://doi.org/10.1007/s11214-013-9965-x

Miura, A. (2007). A magnetospheric energy principle for hydromagnetic stability problems. *Journal of Geophysical Research*, *112*, A06234. doi: https://doi.org/10.1029/2006JA011992

Motoba, T., Ohtani, S., Gkioulidou, M., Ukhorskiy, A. Y., Mitchell, D. G., Takahashi, K., et al. (2018). Response of different ion species to local magnetic dipolarization inside geosynchronous orbit. *Journal of Geophysical Research: Space Physics*, *123*, 5420–5434. doi: https://doi.org/10.1029/2018JA025557

Nakamura, M. S., Matsumoto, H., & Fujimoto, M. (2002). Interchange instability at the leading part of reconnection jets. *Geophysical Research Letters*, *29*(8), 1247. doi: https://doi.org/10.1029/2001GL013780

Nakamura, R., Nagai, T., Birn, J., Sergeev, V. A., Le Contel, O., Varsani, A., et al.

(2017). Near-Earth plasma sheet boundary dynamics during substorm dipolarization. *Earth, Planets and Space*, *69*, 129. doi: https://doi.org/10.1186/s40623-017-0707-2

Nakamura, R., Varsani, A., Genestreti, K. J., Le Contel, O., Nakamura, T., Baumjohann, W., et al. (2018). Multiscale currents observed by MMS in the flow braking region. *Journal of Geophysical Research: Space Physics*, *123*, 1260–1278. doi: https://doi.org/10.1002/2017JA024686

Ohtani, S.-I. (1998). Earthward expansion of tail current disruption: Dual-satellite study. *Journal of Geophysical Research*, *103*, 6815–6825. doi: https://doi.org/10.1029/98JA00013

Paschmann, G., & Daly, P. W. (Eds.). (1998). *Analysis methods for multi-spacecraft data*. Noordwijk, The Netherlands: ESA Publications Division.

Plaschke, F., Kahr, N., Fischer, D., Nakamura, R., Baumjohann, W., Magnes, W., et al. (2016). Steepening of waves at the duskside magnetopause. *Geophysical Research Letters*, *43*, 7373–7380. doi: https://doi.org/10.1002/2016GL070003

Pollock, C., Moore, T., Jacques, A., Burch, J., Gliese, U., Saito, Y., et al. (2016). Fast Plasma Investigation for Magnetospheric Multiscale. *Space Science Reviews*, *199*, 331–406. doi: https://doi.org/10.1007/s11214-016-0245-4

Pritchett, P. L., & Coroniti, F. V. (2010). A kinetic ballooning/interchange instability in the magnetotail. *Journal of Geophysical Research*, *115*, A06301. doi: https://doi.org/10.1029/2009JA014752

Pritchett, P. L., & Coroniti, F. V. (2013). Structure and consequences of the kinetic ballooning/interchange instability in the magnetotail. *Journal of Geophysical Research: Space Physics*, *118*, 146–159. doi: https://doi.org/10.1029/2012JA018143

Reeves, G. D., Kettmann, G., Fritz, T. A., & Belian, R. D. (1992). Further investigation of the CDAW 7 substorm using geosynchronous particle data: Multiple injections and their implications. *Journal of Geophysical Research*, *97*, 6417–6428. doi: https://doi.org/10.1029/91JA03103

Runov, A., Angelopoulos, V., Zhou, X.-Z., Zhang, X.-J., Li, S., Plaschke, F., & Bonnell, J. (2011). A THEMIS multicase study of dipolarization fronts in the magnetotail plasma sheet. *Journal of Geophysical Research*, *116*, A05216. doi: https://doi.org/10.1029/2010JA016316

Russell, C. T., Anderson, B. J., Baumjohann, W., Bromund, K. R., Dearborn, D., Fischer, D., et al. (2016). The Magnetospheric Multiscale magnetometers. *Space Science Reviews*, *199*, 189–256. doi: https://doi.org/10.1007/s11214-014-0057-3

Saito, M. H., Miyashita, Y., Fujimoto, M., Shinohara, I., Saito, Y., Liou, K., & Mukai, T. (2008). Ballooning mode waves prior to substorm-associated dipolarizations: Geotail observations. *Geophysical Research Letters*, *35*, L07103. doi: https://doi.org/10.1029/2008GL033269

Schmid, D., Volwerk, M., Plaschke, F., Nakamura, R., Baumjohann, W., Wang, G. Q., et al. (2019). A statistical study on the properties of dips ahead of dipolarization fronts observed by MMS. *Journal of Geophysical Research: Space Physics*, *124*, 139–150. doi: https://doi.org/10.1029/2018JA026062

Stix, T. H. (1992). *Waves in plasmas*. Berlin, Germany: Springer.

Torbert, R. B., Vaith, H., Granoff, M., Widholm, M., Gaidos, J. A., Briggs, B. H., et al. (2016). The Electron Drift Instrument for MMS. *Space Science Reviews*, *199*, 283–305. doi: https://doi.org/10.1007/s11214-015-0182-7

Winske, D. (1996). Regimes of the magnetized Rayleigh-Taylor instability. *Physics of Plasmas*, *3*, 3966–3974. doi: https://doi.org/10.1063/1.871569

Wolf, R. A., Kumar, V., Toffoletto, F. R., Erickson, G. M., Savoie, A. M., Chen, C. X., & Lemon, C. L. (2006). Estimating local plasma sheet $PV^{5/3}$ from single-spacecraft measurements. *Journal of Geophysical Research*, *111*, A12218. doi: https://doi.org/10.1029/2006JA012010

Wygant, J. R., Bonnell, J. W., Goetz, K., Ergun, R. E., Mozer, F. S., Bale, S. D., et al. (2013). The Electric Field and Waves instruments on the Radiation Belt Storm Probes mission. *Space Science Reviews*, *179*, 183–220. doi: https://doi.org/10.1007/s11214-013-0013-7

Young, D. T., Burch, J. L., Gomez, R. G., De Los Santos, A., Miller, G. P., Wilson, P., IV, et al. (2016). Hot Plasma Composition Analyzer for the Magnetospheric Multiscale mission. *Space Science Reviews*, *199*, 407–470. doi: https://doi.org/10.1007/s11214-014-0119-6